Journal of Colloid and Interface Science 686 (2025) 660–671

Contents lists available at ScienceDirect

Journal of Colloid And Interface Science

journal homepage: www.elsevier.com/locate/jcis

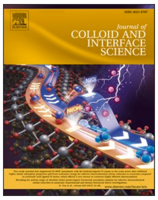

Regular Article

An integrated optimization strategy by Joule heating technique enabling rapid fabrication of robust $Li_{1.3}Al_{0.3}Ti_{1.7}(PO_4)_3$ solid-state electrolyte for all-solid-state lithium metal batteries

Xiangming Cui, Xin Chen, Changzheng Lin, Jingzhao Wang, Zirui Guo, Mi Zhou, Zhouzhou Yao, Jiaxin Zhang, Shiyi Sun, Jianan Wang *, Wei Yan

Department of Environmental Science and Engineering, School of Energy and Power Engineering, Xi'an Jiaotong University, Xi'an 710049 PR China

GRAPHICAL ABSTRACT

Sintering auxiliaries and dual-process sintering approach enables rapid densification of LATP SSEs. The thermal pulse welding technique further improves interfacial contact between the SSE and electrodes, significantly improving ASSLMBs' electrochemical performance.

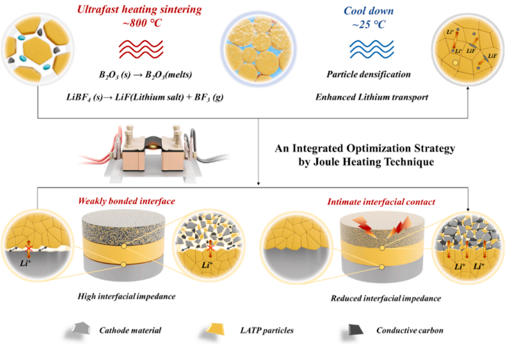

ARTICLE INFO

Keywords:
Solid-state batteries
Solid-state electrolyte
Joule heating
Optimization strategy

ABSTRACT

The advancement of high-energy–density and intrinsically safe all-solid-state lithium metal batteries (ASSLMBs) is crucial for the comprehensive electrification of energy consumption. Nevertheless, intrinsic defects in solid-state electrolytes (SSEs) and suboptimal interfacial contacts often lead to uncontrolled dendritic growth during practical battery operation. To address these challenges, this study proposes an integrated optimization strategy for bulk-phase defects and interfacial contacts of $Li_{1.3}Al_{0.3}Ti_{1.7}(PO_4)_3$ (LATP) SSEs based on ultra-fast Joule heating sintering (UHS) technique. Introducing specific sintering auxiliaries and a dual-process sintering approach can achieve the rapid densification of LATP SSEs. Additionally, the thermal pulse welding (TPW) technique for the integrated anode/SSE/cathode further provides superior SSE/electrode interface contact, facilitating the in-situ formation of a continuous ion-conducting network for improved electrochemical kinetics. The optimized Li||LATP||NCM811 ASSLMBs demonstrate exceptional specific capacity (185.9 mAh/g at 0.2 C) and robust cycling stability (90.9 % capacity retention after 100 cycles). This integrated optimization strategy can offer a critical technical reference for the rapid fabrication of high-performance ASSLMBs.

---

* Corresponding author.
E-mail address: wangjn116@xjtu.edu.cn (J. Wang).

https://doi.org/10.1016/j.jcis.2025.01.276
Received 30 October 2024; Received in revised form 13 January 2025; Accepted 31 January 2025
Available online 1 February 2025
0021-9797/© 2025 Elsevier Inc. All rights are reserved, including those for text and data mining, AI training, and similar technologies.

1. Introduction

The global energy crisis, marked by shortages and excessive carbon emissions, has initiated a transformative shift in energy production and consumption [1]. Developing highly efficient electrochemical energy storage devices with higher energy densities becomes increasingly crucial for future low-carbon and multi-energy-integrated society [2]. Such devices include alkali metal batteries, fuel cells, and solid-state batteries, which are at the forefront of addressing challenges in the ongoing energy revolution [3–5]. Among them, all-solid-state lithium metal batteries (ASSLMBs) have gained significant attention due to their potential to achieve high energy density and enhanced safety. These batteries employ solid-state electrolytes (SSEs) composed of ion-conducting materials, coupled with lithium metal anodes (specific capacity ~ 3860 mAh/g, redox potential ~ 3.04 versus standard hydrogen electrode, SHE) and high-voltage cathodes (such as nickel-rich or high-voltage spinel materials) [6,7]. Despite their promise, the practical application of ASSLMBs still faces major challenges, particularly the uncontrolled growth of lithium dendrites.

Defects within the bulk phase of SSEs and poor interfacial contacts are two key factors contributing to lithium dendrite growth. Internal defects of SSEs, such as voids, cracks, and electron-conductive grain boundaries, create favorable thermodynamic conditions for irregular lithium nucleation within SSEs [8]. Furthermore, poor interfacial contact between SSEs and electrode also easily leads to uneven lithium-ion transport and inhomogeneous current density distribution, accelerating the growth of lithium dendrites to penetrate the SSEs [8,9]. The formation of lithium dendrites both on the surface and within the bulk of SSEs results in battery capacity degradation and structural failure of SSEs, ultimately causing significant safety risks [10,11]. Numerous studies have demonstrated that both enhancing the bulk properties of SSEs (e.g., density, crystallinity, and ionic conductivity) and optimizing the SSE/electrode interfacial contact are effective strategies to address these issues and enhance the electrochemical performance of ASSLMBs [12–15].

In the family of SSEs, $Li_{1+x}Al_xTi_{2-x}(PO_4)_3$ (LATP, $x = 0.3–0.5$), as a typical oxide-based electrolyte, is widely used in ASSLMBs due to its low sintering temperature, high ionic conductivity(10^{-3} to 10^{-4} S cm^{-1}), voltage tolerance (~6 V) and environmental stability [16,17]. However, conventional high-temperature sintering (CHST) often leads to significant bulk-phase defects during the fabrication of LATP SSEs, such as non-uniform microstructures and suboptimal ionic transport pathways. Prolonged sintering induces crystallographic changes, phase segregation and lithium volatilization, compromising lattice stability and reducing ionic conductivity [18,19]. In contrast, the ultra-fast Joule heating sintering (UHS) technique, known for its rapid, cost-effective and controllable 'flash sintering,' can efficiently enhance crystallization and densification of SSEs while mitigating lithium volatilization and phase changes [20]. Nonetheless, the intense temperature variations and thermal transfer induced by UHS inevitably result in uneven thermal expansion of the ceramic particles, generating internal stresses that hinder effective particle diffusion and structural reorganization [21]. To address these issues and optimize the bulk properties of SSEs, introducing specific sintering auxiliaries suitable for UHS will be a feasible solution to enhance the densification of SSE bulk structures and prevent dendrite penetration.

Furthermore, the conventional physical stacking (CPS) method for anode/SSE/cathode hardly achieves effective microscopic contact between the electrodes and the SSE, always emerging as a significant factor in the degradation of ASSLMBs [14,22]. The incorporation of a flexible buffer layer at the SSE/electrode interface offers a feasible solution to optimize this interface problem. However, it generally compromises the thermal stability of the battery and may induce adverse reactions under high-voltage conditions [23,24]. Although in-situ alloying reactions can establish a functional SSE/electrode interface, this method is inherently complex and difficult to control reliably [25,26]. Given that UHS can achieve rapid densification of crystalline materials without inducing unnecessary phase diffusion, the development of a UHS-based integrated interface welding technique for anode/SSE/cathode to resolve interface issues in ASSLMBs represents a highly advantageous solution [20].

Herein, an integrated optimization strategy has been proposed to simultaneously address the bulk-phase defects in LATP SSEs and the interfacial contacts in ASSLMBs. For the optimization of bulk-phase defects, a high-performance LATP SSE is realized through a novel ultrafast Joule heating sintering (NUHS) technique, which includes a dual-process sintering approach (pre-heat annealing and ultra-fast Joule heating treatment) with B_2O_3 (a liquid-phase sintering agent) and $LiBF_4$ (an ionic additive) incorporating into LATP powders as sintering auxiliaries. For the optimization of interfacial contacts, the thermal pulse welding (TPW) technique is employed for the integrated anode/SSE/cathode to enable tight interface contact. As a result, the LATP SSEs derived from NUHS-TPW exhibit superior crystallinity and densification compared to those produced through conventional high-temperature sintering (CHST) and conventional ultra-fast Joule heating techniques (CUHS), along with robust thermo-mechanical stability and resistance to stress erosion. The produced ASSLMBs by NUHS-TPW also demonstrate rapid reaction kinetics, high initial capacity and robust cycling stability under different operating temperatures.

2. Experimental materials/methods

2.1. Materials

All chemicals utilized were of analytical grade and did not require any further purification. Ammonium dihydrogen phosphate ($NH_4H_2PO_4$), alumina (Al_2O_3), titanium dioxide (TiO_2), lithium nitrate ($LiNO_3$), isopropanol (C_3H_8O), anhydrous ethanol (C_2H_5OH), urea (CH_4N_2O) and *N*-methyl-2-pyrrolidone (NMP) were obtained from Aladdin. Boron oxide (B_2O_3) and lithium tetrafluoroborate ($LiBF_4$) were obtained from Agilent. Aluminum foil, conductive carbon black, lithium foil, polyvinylidene fluoride (PVDF), lithium iron phosphate cathode ($LiFePO_4$, LFP), and nickel–cobalt-manganese oxide cathode ($LiNi_{0.8}Co_{0.1}Mn_{0.1}O_2$, NCM811) were obtained from Canrd.

2.2. Synthesis method of LATP precursor powders

The preparation of LATP precursor powders was performed by conventional high-temperature solid-state synthesis method. Firstly, stoichiometric amounts of lithium nitrate ($LiNO_3$), aluminum oxide (Al_2O_3), titanium dioxide (TiO_2), and ammonium dihydrogen phosphate ($NH_4H_2PO_4$) at a molar ratio of 1.3:0.15:1.7:3 were weighed accurately. The pre-weighed powders were then introduced into a ball milling jar, along with a suitable amount of isopropanol. The sealed ball mill jar was subjected to milling at 50 rpm for 8 h. Following this, the mixture was transferred to an oven and dried at 80°C for 6 h to ensure complete evaporation of isopropanol. The dried powders were subsequently transferred to a muffle furnace for calcination, with the temperature being ramped from room temperature to 800 °C at a rate of 5 °C/min. Following a 6-hour dwell at 800 °C, the temperature was decreased to room temperature at a rate of 5 °C/min. The dried powders were transferred to a vibrating sieve machine and screened through 200-mesh and 400-mesh standard sieves to achieve LATP precursor powders with consistent particle size and minimal agglomeration. The obtained powders are shown in **Fig. S1**.

2.3. Fabrication method of LATP solid-state electrolytes (SSEs)

Conventional High-Temperature Sintering Technique (CHST): The LATP precursor powders were placed within a metal mold and pressed into a ceramic green body under 10 MPa of pressure using a hydraulic press. The ceramic green body was situated in a crucible, with the surface embedded in LATP precursor powders, and then transferred to a muffle furnace for high-temperature sintering. The temperature was elevated from room temperature to 950 °C at a rate of 5 °C/min, held at 950 °C for 6 h, cooled from 950 °C to 750 °C at 2 °C/min, and finally cooled to room temperature at 5 °C/min. Before battery assembly, the LATP SSEs were subjected to grinding and polishing on a metallographic polishing machine. After further cleaning with ethanol, the LATP SSEs prepared by CHST were obtained (LATP-CHST).

Conventional Ultrafast Joule Heating Sintering (CUHS): The compressed LATP ceramic green slice was placed in the Joule heating apparatus and annealed (120 s) with a 32 V voltage, a 20 A heating current and a sintering temperature threshold of 900 °C under N_2 atmosphere. After the Joule-heating process was completed, the sample was cooled gradually to room temperature. After grinding, polishing and cleaning with ethanol, the LATP SSEs prepared by CUHS were obtained (LATP-CUHS).

Novel Ultrafast Joule Heating Sintering (NUHS): The LATP precursor powders, along with B_2O_3 powder (2 wt%) and $LiBF_4$ powder (0.5 wt%), were mixed and placed into a ball milling jar with an appropriate quantity of isopropanol. After sealing, the jar was ball milled at 50 rpm for 8 h, and the mixture was then transferred to an oven and dried at 80 °C for 6 h, ensuring the complete evaporation of the isopropanol. The dried powders were placed into a metal mold and then compressed under a pressure of 10 MPa using a hydraulic press to form a ceramic green slice. The ceramic green slice was transferred into a tube furnace and **s**ubjected to pre-annealing treatment at 750 °C for 2 h, and then was subsequently placed into the Joule heating apparatus (as depicted in **Fig. S2**) for annealing (120 s) with a voltage of 32 V, a current of 20 A and a sintering temperature limit of 800 °C under N_2 atmosphere. After cooling, grinding, polishing and cleaning with ethanol, the LATP SSEs prepared by NUHS were obtained (LATP-NUHS).

2.4. Fabrication method for Li||LATP||LFP and Li||LATP||NCM811 batteries

CR2032 coin cells were assembled in an argon-filled glove box (Dellix LS750S, China), where humidity and oxygen levels were maintained below 0.1 ppm. The NCM811 or LFP cathodes were synthesized via a doctor-blade coating method on LATP SSE without using a current collector, resulting in LATP-LFP pellet and LATP-NCM811 pellet. The LATP pellet with the coated cathode was assembled with lithium foil to form a tri-layer 'anode/SSE/cathode' sandwich structure. The sandwich structure was encapsulated into a CR2032 coin cell casing within a glove box to complete the assembly of the lithium metal solid-state battery.

LFP cathode on the LATP SSE (LATP-LFP pellet): The LFP cathode was prepared through a method involving the pre-mixing of LFP powders, conductive carbon black, LATP powders and PVDF powders in a weight ratio of 70:10:15:5. This powder mixture was then transferred to an NMP solvent (with a solid content of about 35 wt%) and stirred vigorously on a magnetic stirrer for 24 h. The resulting homogeneous LFP slurry was evenly coated on one side of the LATP SSE (~100 μm) and dried.

NCM811 cathode on the LATP SSE (LATP-NCM811 pellet): The process for preparing the NCM811 cathode by mixing NCM811 powders, conductive carbon black, LATP powders and PVDF powders in a 70:10:15:5 wt ratio. This mixture was then added to an NMP solvent (with a solid content of ~ 30 wt%) and stirred vigorously for 24 h using a magnetic stirrer. The well-dispersed NCM811 slurry was evenly spread (~100 μm) over one side of the LATP SSE and dried.

Fabrication of the tri-layer 'anode/SSE/cathode' sandwich structure: For the CHST and CUHS methods, the sandwich structure was formed by tightly bonding the LATP pellet with the cathode to the lithium foil, with no further treatment required. In contrast, for the NUHS method, the sandwich structure, after bonding the lithium foil to the LATP pellet, was placed into a sealed fixture and transferred to the Joule heating device for thermal pulse welding. The structure underwent three thermal pulses at 200 °C in a nitrogen atmosphere, achieving a tightly bonded interface.

2.5. Fabrication of silver paste (SP)/LATP/SP batteries

For evaluating the lithium-ion conductivity of the LATP membrane, high-temperature SP was applied uniformly to both surfaces of the LATP pellet. After high-temperature drying, symmetric SP/LATP/SP blocking batteries were assembled. Electrochemical impedance spectroscopy (EIS) was used to measure the electrochemical AC impedance of SSEs across a frequency spectrum of 0.01–1 MHz, enabling the calculation of their ionic conductivity.

$$\sigma = \frac{h}{RA} \tag{1}$$

In the equation, σ indicates the lithium-ion conductivity (S cm^{-1}); h represents the thickness of the sample (cm); R is the impedance of the sample (Ω); and A refers to the surface area of the blocking electrode (cm^2).

Furthermore, EIS tests of LATP SSE at different temperatures enable the calculation of the lithium-ion activation energy using the Arrhenius equation. The ionic conductivity (σ) at different temperatures follows the Arrhenius relationship:

$$\sigma = \sigma_0 \exp\left(-\frac{E_a}{kT}\right) \tag{2}$$

In the equation, E_a is the activation energy. σ_0 is the pre-exponential factor; k represents the Boltzmann constant (8.617×10^{-5} eV/K); T is the absolute temperature (K).

2.6. Fabrication of Li/LATP/Stainless steel (SS) batteries

To assess the electrochemical stability window of SSEs, Li/LATP/SS batteries were fabricated in an Ar-filled glove box, with the SSEs placed between lithium foil and stainless steel electrodes. Linear sweep voltammetry (LSV) was conducted on these batteries over a 2.5–6.0 V range at a scan rate of 1 mV/s.

2.7. Fabrication of lithium (Li) /LATP/Li batteries

To determine the lithium-ion transference number (t_{Li^+}) of SSEs, Li/LATP/Li batteries were assembled in an Ar-filled glove box, with SSEs placed between two lithium metal anodes. EIS and chronoamperometry tests were performed following the Bruce-Vincent method. The transference number was calculated using the following formula:

$$t_{Li^+} = \frac{I_s(\Delta V - I_0 R_0)}{I_0(\Delta V - I_s R_s)} \tag{3}$$

Where ΔV is the amplitude of applied polarization (10 mV).I_0 and R_0 represent the current and interfacial resistance at the initial state without polarization, respectively. Correspondingly, I_s and R_s are the parameters at the steady state.

2.8. Characterization

The morphological analysis of SSEs was conducted using field-emission scanning electron microscopy (FE-SEM) (Gemini SEM500), and elemental mapping of the material surface was performed using energy-dispersive X-ray spectroscopy (EDS). The crystalline structure and composition of the samples were characterized using X-ray diffraction (XRD) (PANalytical X'pert MPDPro, Netherlands), with CuKα radiation (λ = 1.5418 Å, 40 kV, 40 mA) providing the diffraction patterns. The affinity of the samples towards the electrolyte was tested using a contact angle goniometer (Kruss DSA100 635, Germany). Phase content quantification was carried out using Jade 9, with phase identification and profile fitting tools used to determine the crystallinity of the samples. The crystallinity was expressed as the ratio of the crystalline diffraction peaks' intensity to the sum of the diffraction and scattering peaks' intensities.

$$C = \frac{I_d}{I_t} \tag{4}$$

In this context, C represents the crystallinity, I_d denotes the intensity of diffraction peaks, and I_t refers to the total intensity of the diffraction and scattering peaks.

The microcrystalline size of the sample was calculated using the Debye-Scherrer equation, as presented below:

$$D = \frac{0.89\lambda}{\beta cos\theta} \tag{5}$$

In this formula, D represents the average size of the crystallites (nm); λ is the wavelength of Cu Kα radiation (nm); β is the full width at half maximum (FWHM) in radians (rad); and θ is the diffraction angle in degrees (°).

Mechanical puncture tests were performed using a universal testing machine (CMT4000, China) with a compression speed of 3 mm/min. The internal structure of the SSE was obtained using X-ray computed tomography (Thermo Scientific Helios 5 UX). Surface roughness and Young's modulus of the SSEs were measured by atomic force microscopy (SPM-9700HT), and surface thermal distribution was assessed using an infrared thermal imaging camera (Fotric 615C). The surface contact angle measurements of the SSEs were conducted using a contact angle goniometer (JC200D1). The surface free energy of the SSEs was measured using the Owens-Wendt two-liquid method, with the surface free energy calculated based on the contact angles of water and diiodomethane on the surface of the SSEs.

To determine the Li^+ diffusion coefficient, cyclic voltammetry (CV) tests were conducted on Li/LATP/LFP batteries at various scan rates (0.1–0.5 mV/s). The Li^+ diffusion coefficient was calculated using the following Randles-Sevcik equation:

$$I_p = 2.69 \times 105 \times n^{3/2} \times A \times D^{1/2} \times \vartheta^{1/2} \times C_0 \tag{6}$$

where I_p is the peak current, n is the number of electrons involved in the redox process, A is the electrode area, D is the Li^+ diffusion coefficient, C_0 is the Li^+ concentration, and ϑ is the scan rate. Fitting the relationship between the peak current and the square root of the scan rate allowed the derivation of the Li^+ diffusion coefficients for the three LATP SSEs.

Charge and discharge experiments were performed with a Neware battery testing system within the voltage windows of 2.8–4.2 V (vs. Li/Li) for NCM811 batteries and 2.5–3.8 V (vs. Li/Li) for LFP batteries. EIS tests were conducted over a frequency range from 0.01 to 10 kHz.

3. Results and discussion

Regarding the bulk densification of LATP SSEs during the conventional ultrafast Joule heating process, abrupt temperature changes and non-uniform heat transfer generate significant internal stresses, impeding the ordered diffusion and restructuring of particles [21,27,28]. By adding a suitable amount of B_2O_3 (a liquid-phase sintering agent) and $LiBF_4$ (an ionic additive) powders to the LATP precursor, the internal stress during sintering can be minimized and consequently improving the bulk density of LATP SSEs [29,30]. As shown in Fig. 1**a**, when the LATP particles retain their crystalline shape and expand during heating, the molten B_2O_3 acts as a 'lubricant' to facilitate the diffusion and realignment of particles. $LiBF_4$ fills the voids and converts to LiF with elevated temperatures, promoting grain boundary fusion and replenishing lithium loss [31]. As shown in Fig. 1**b, 1c and 1d**, after pre-annealing treatment at ~ 750 °C for 2 h to ensure the additives to uniformly distribute around the LATP particles, ultrafast Joule heating (~120 s, 32 V, 20 A) was performed. Notably, the separate use of B_2O_3 or $LiBF_4$ could cause wide or irregular grain boundaries, as seen in **Fig. S3**. The optimized powder formulation, along with the special dual heat treatment in the NUHS process, results in LATP SSEs with improved bulk densification and superior ionic conductivity. Furthermore, the TPW (~22 s, ~750 °C) technique, as shown in the heating curve in **Fig. S4**, enables rapid anode/LATP/cathode bonding at the micro scale, preventing lithium spillage and phase changes in the SSEs [32]. The optimized interface could also reduce ionic transport distances and enhanced interfacial lithium-ion transport (Fig. 1**e and 1f**). In conclusion, advancements in sintering and process optimization are able to produce robust LATP SSEs (bulk-phase strategy) and improved SSE/electrode interfaces (interface strategy) for high-performance ASSLMBs.

To evaluate the effectiveness of NUHS, the morphology and structure of LATP SSEs fabricated via CHST, CUHS and NUHS were analyzed (their preparation processes are also illustrated in **Fig. S5**). LATP-CUHS SSE exhibited internally well-ordered ceramic microstructures, yet conspicuous voids among particles were still observed with irregular grain growth patterns across various regions (Fig. 2**a**). These substantial voids acted as barriers to lithium-ion transportation across grains, thereby constraining the efficacy of ionic diffusion pathways. This phenomenon likely arose from the uneven thermal diffusion and abrupt temperature gradients, creating heterogeneous heating environments, impeding controlled grain growth [27,28]. In Fig. 2**b**, the surface of LATP-CHST SSE was coated with irregular paste-like residues, potentially attributed to the decomposition of secondary phases induced by prolonged high-temperature sintering [31,33]. In comparison, LATP SSE synthesized by NUHS (LATP-NUHS) exhibited a compact and uniform surface microstructure. The ceramic particles were tightly bonded by liquid-phase sintering agents (Fig. 2**c**), enabling a notable reduction in intergranular impedance, as illustrated in **Table S1**. Additionally, EDS mapping (**Fig. S6**) revealed a homogeneous distribution of Li, Ti, Al, P, B and O elements within the LATP-NUHS SSE, which were instrumental in achieving uniform particle alignment and reinforcing grain boundary consolidation.

The defect ratios and crystal structure of various samples were further investigated to assess the effects of NUHS on the internal structure of LATP SSEs. X-ray computed tomography (X-CT) and 3D reconstruction techniques were first employed to characterize the defects within various LATP SSEs. Detected defects larger than 1 μm^3 (including pores, voids and cracks) were size-color-coded in the reconstructed images. As shown in Fig. 2**d and 2e**, both LATP-CUHS and LATP-CHST exhibited numerous defect regions with total defect rates of 5.68 % and 2.67 %, respectively. According to the normalized defect size distribution calculation in **Fig. S7a and S7b**, LATP-CUHS had the highest defect number among these three samples, including 72.86 % small pores ranging from 1 to 1.0×10^1 μm^3, 16.97 % voids ranging from 1.0×10^1 to 1.0×10^2 μm^3, and 10.17 % large cracks ranging of $> 1.0 \times 10^2$ μm^3. This result was mainly attributed to the fact that the ultra-fast Joule heating sintering could hardly provide enough time for grain growth and grain boundary healing [34]. Although LATP-CHST exhibited a reduced defect number compared with LATP-CUHS, the conventional high-temperature sintering will induce the formation of a higher percentage of voids (44.44 %) and large cracks (22.17 %). The larger defect size could increase the risk of stress-induced failure and dendrite penetration for SSEs. By comparison, as depicted in Fig. 2**f and Fig. S7c**, LATP-NUHS after bulk-phase optimization exhibited the lowest total defect rate of only 0.01 % and the fewest defects, composed almost entirely of small holes (99.83 %), demonstrating the high structural densification of LATP-NUHS as well as the effectiveness of the introduced sintering auxiliaries and the dual-process sintering approach.

XRD analysis of the LATP SSEs revealed that the main diffraction peaks of these three LATP SSEs and LATP precursor powders corresponded well with the standard XRD patterns of $LiTi_2(PO_4)_3$ with NASICON-type structure (Fig. 2**g and Fig. S8**), confirming the synthesis of pure-phase and high-crystallinity LATP SSEs [35]. The slight

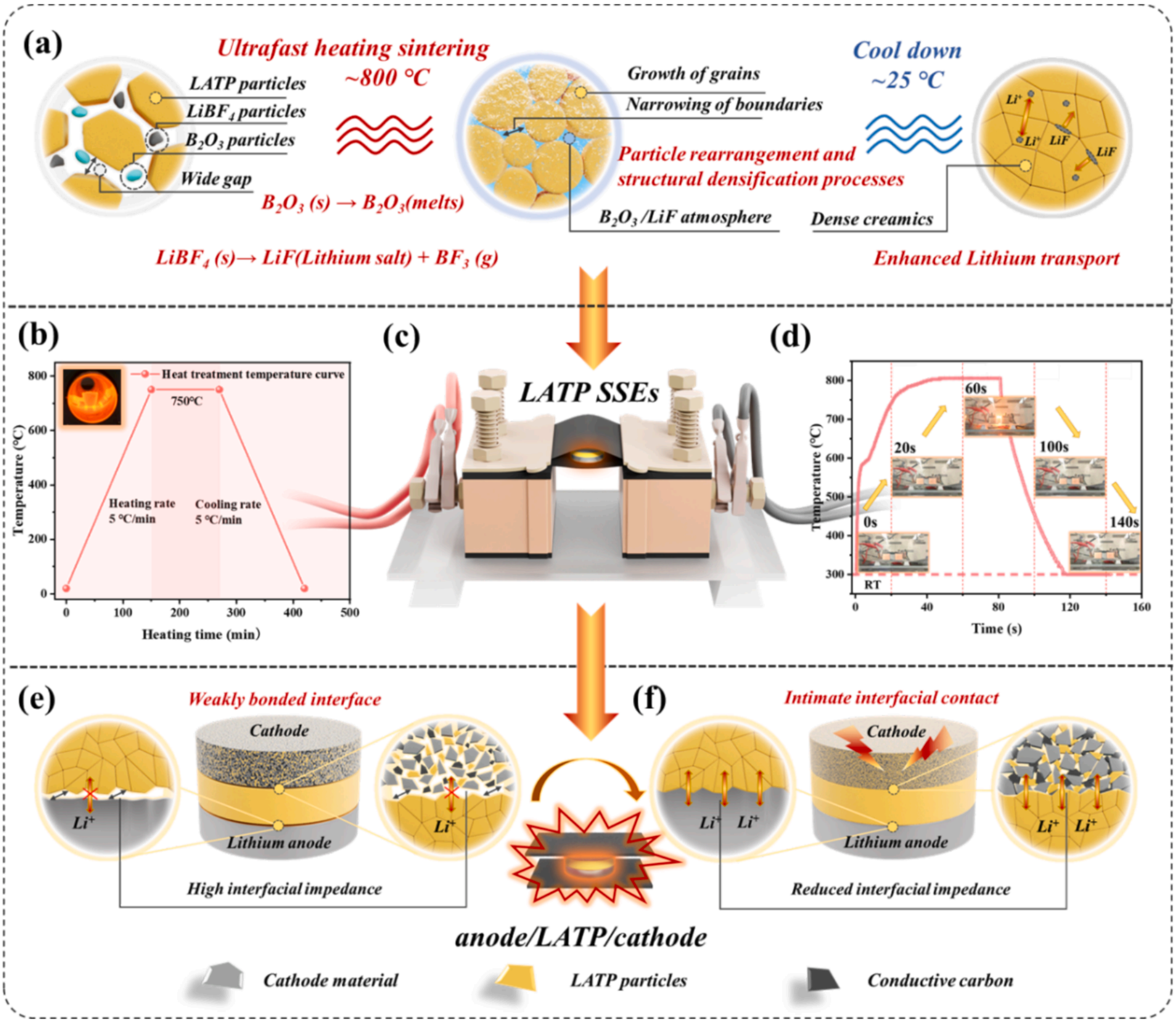

Fig. 1. Schematic of the integrated optimization strategies for bulk and interface using the UHS. a) The incorporation of liquid-phase sintering agent and ionic additive for bulk phase optimization of the LATP SSEs. b) Pre-annealing procedure. c) Schematic of the Joule heating apparatus for LATP SSEs. d) High-temperature synthesis procedure using ultra-fast Joule heating sintering technique. Schematic of TPW technique for integrated anode/SSE/cathode. e) The conventional physical stacking approach. f) The TPW approach for integrated anode/SSE/cathode.

deviations observed in the XRD patterns of LATP-NUHS and LATP-CUHS compared to the standard $LiTi_2(PO_4)_3$ could result from the sintering auxiliaries. According to further analysis using Jade 9.0 software, the average microcrystal sizes of LATP-CUHS, LATP-CHST and LATP-NUHS in the primary diffraction peak directions including (104), (113), (024), (211), (116), (300), (223), (134), (042) and (410) were calculated as 51.62 nm, 60.69 nm and 51.38 nm, respectively (Fig. 2**h**), presenting significant grain growth compared to the LATP precursor powders (33.93 nm) [36]. Although LATP-CUHS and LATP-CHST possessed the larger microcrystal size compared to LATP-NUHS, due to the presence of more voids and cracks, their crystallinity and relative LATP phase content were lower than those of LATP-NUHS (98.99 % and 96.26 %) (Fig. 2**i**).

To gain a more comprehensive insight into the NUHS mechanism, the structural evolution of LATP-NUHS throughout the Joule heating sintering preparation process was dynamically monitored. NUHS consists of two key steps: pre-annealing step and UHS step. In this study, SEM was used to monitor the structural changes of LATP SSE during these two steps. As shown in **Fig. S9 and S10**, compared to LATP SSEs without any heat treatment, the densification of LATP SSEs was moderately improved after pre-annealing step, with the liquid-phase sintering agent and ionic additive tightly bonding the ceramic particles together. During the melting sintering stage (~800°C) of the UHS step, the LATP particles in the early stage of melting sintering (1 s) possessed a smooth surface and no particle encapsulation was observed (Fig. 3**a**), suggesting that volatile impurities were effectively removed under ultrafast heating. The particles were driven by surface energy to re-diffuse and rearrange with the onset of necking phenomena [37]. As shown in Fig. 3**b**, the particles were surrounded by some uniformly solidified glassy phase materials, which were detected by EDS to be a mixture of B_2O_3 and LiF, serving lubricating and densification functions (**Fig. S11**). During the mid-stage of melting sintering (15 s), the LATP particles were melted and adhered together but some pores still were remained (Fig. 3**c**). Internal grains aggregated into larger crystals, grew directionally and expelled voids with the aid of sintering auxiliaries, thereby gradually enhancing the densification of LATP SSE during this stage (Fig. 3**d**). Notably, as the sintering process was driven by the reduction of surface energy, LATP preferentially grew along the (113) crystal plane with the lowest surface energy [32]. In the final stage of Melting Sintering (30 s), distinct grain boundaries were observed among the ceramic particles (Fig. 3**e**), with internal grains adhering closely and regular morphology (Fig. 3**f**), suggesting the successful formation of high-densification LATP SSE by NUHS technique.

The thermal and mechanical stabilities of various LATP SSEs and

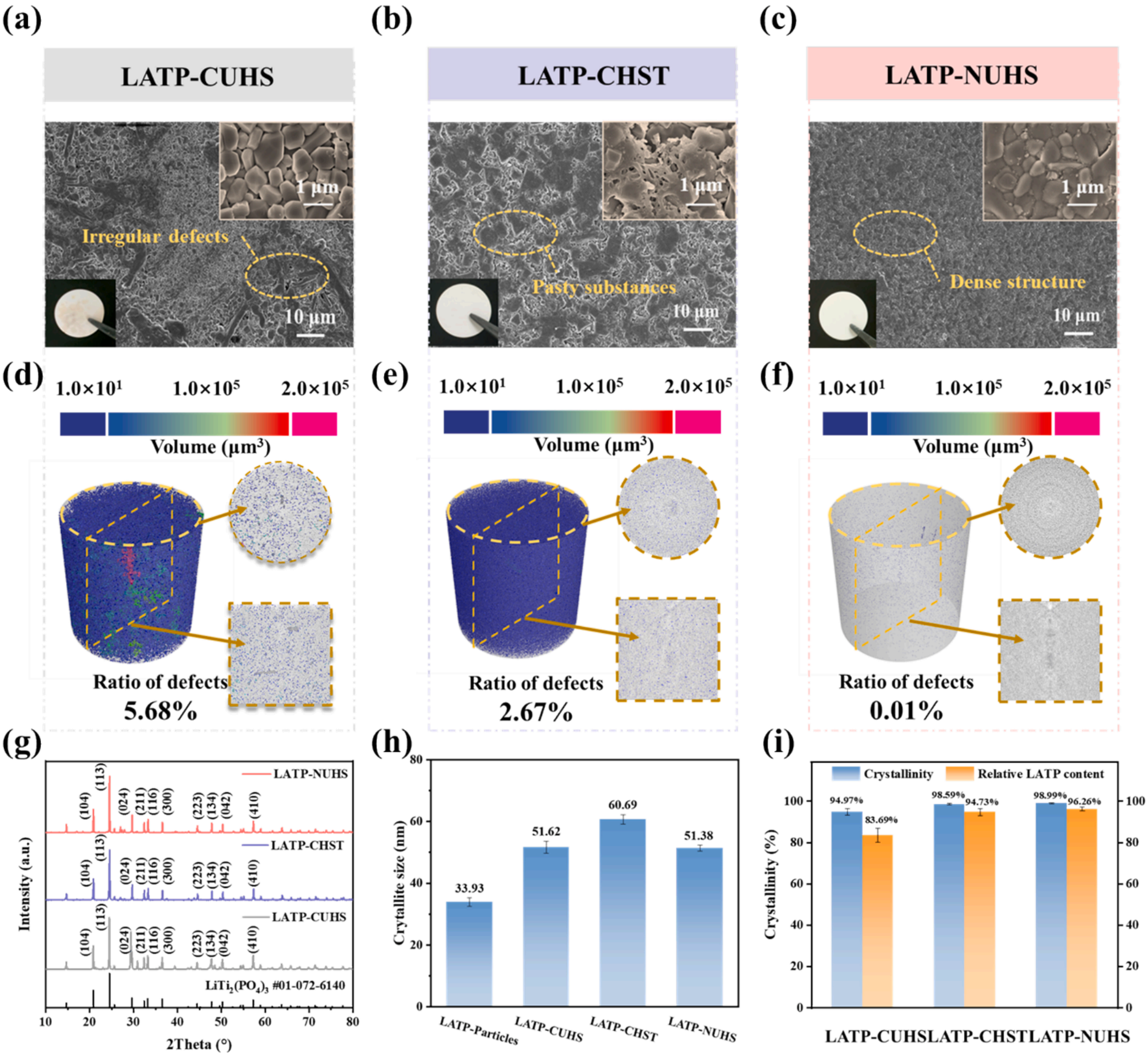

Fig. 2. Surface morphology and structural analysis of various LATP SSEs. a-c) SEM and optical images of LATP-CUHS, LATP-CHST and LATP-NUHS. d-f) Internal structure imaging for LATP-CUHS, LATP-CHST and LATP-NUHS based on X-CT. g) XRD patterns. h) Microcrystalline sizes of LATP powder and various LATP SSEs. i) Crystallinity and effective phase content of LATP SSEs. Three times repeated experiments were carried out and the error bars were shown in Fig. 2h and 2i.

their surface robustness were evaluated as shown in Fig. 4. An infrared thermographic system was utilized to monitor the surface thermal distribution of LATP SSEs under extreme temperatures ranging from 100 to 200 °C. LATP-NUHS achieved a uniform and stable thermal distribution at both 100°C and 200 °C without 'hotspots' being observed (Fig. 4**a**). In contrast, LATP-CHST and LATP-CUHS exhibited more 'hotspots' zones due to heat accumulation and uneven heat transfer resulting from their bulk-phase defects (Fig. 4**b and 4c**). In particular, numerous 'hotspots' even existed at a heating condition of 100 °C in LATP-CUHS, likely due to its high defect number and low crystallinity as explained in Fig. 2. These 'hotspots' could induce the selective deposition/distribution of lithium ions during charging and discharging of ASSLMBs, creating thermodynamic conditions to accelerate the growth of lithium dendrites [38,39]. The thermal ignition test in **Fig. S12** further revealed the non-flammable nature of LATP-NUHS. The surface free energies of various LATP SSEs were measured by contact angle test using water and diiodomethane as testing liquids (**Fig. S13)**. The highest surface free energy of LATP-NUHS (75.84 mN m^{-1}) among these three LATP SSEs also implied its highest interface affinity toward electrodes [40]. Moreover, the root mean square roughness (R_a) of LATP SSEs was quantified using atomic force microscopy (AFM). LATP-NUHS exhibited the lowest average root mean square roughness (14.2 ± 2.4 nm) compared to LATP-CHST (66.1 ± 3.2 nm) and LATP-CUHS (137.2 ± 10.7 nm) (Fig. 4**d**). The AFM surface images of LATP SSEs revealed that LATP-NUHS had a smooth surface (**Fig. S14**), while LATP-CHST and LATP-CUHS displayed visible voids on their surfaces, consistent with the observations from SEM. The smooth surface facilitates the wettability of LATP SSE to lithium, preventing uneven lithium deposition caused by current focusing [41].

The bulk optimization strategy for LATP SSEs can significantly enhance the densification and crystallinity. To assess the ionic conductivity and the effects of the interface optimization strategy on battery performance, electrochemical impedance spectroscopy (EIS) was performed on the LATP SSEs and corresponding solid-state batteries before and after applying the TPW technique. As shown in Fig. 5**a**, the EIS curves for a silver paste (SP)||LATP||SP battery configuration were firstly presented to highlight the key impedance characteristics of various SSEs. The EIS spectra revealed two R-C semicircles in the high-frequency and mid-frequency regions. For NASICON-type solid-state electrolytes, these two R-C semicircles correspond to the contributions of the grain bulk (R_{bulk}) and grain boundary (R_{gb}) to the ionic impedance, respectively. The total impedance (R_{tot}) comprises R_{bulk} and R_{gb} [42,43]. The low-frequency semi-infinite diffusion line indicated lithium-ion blocking at the SSE/electrode interface, as illustrated by the

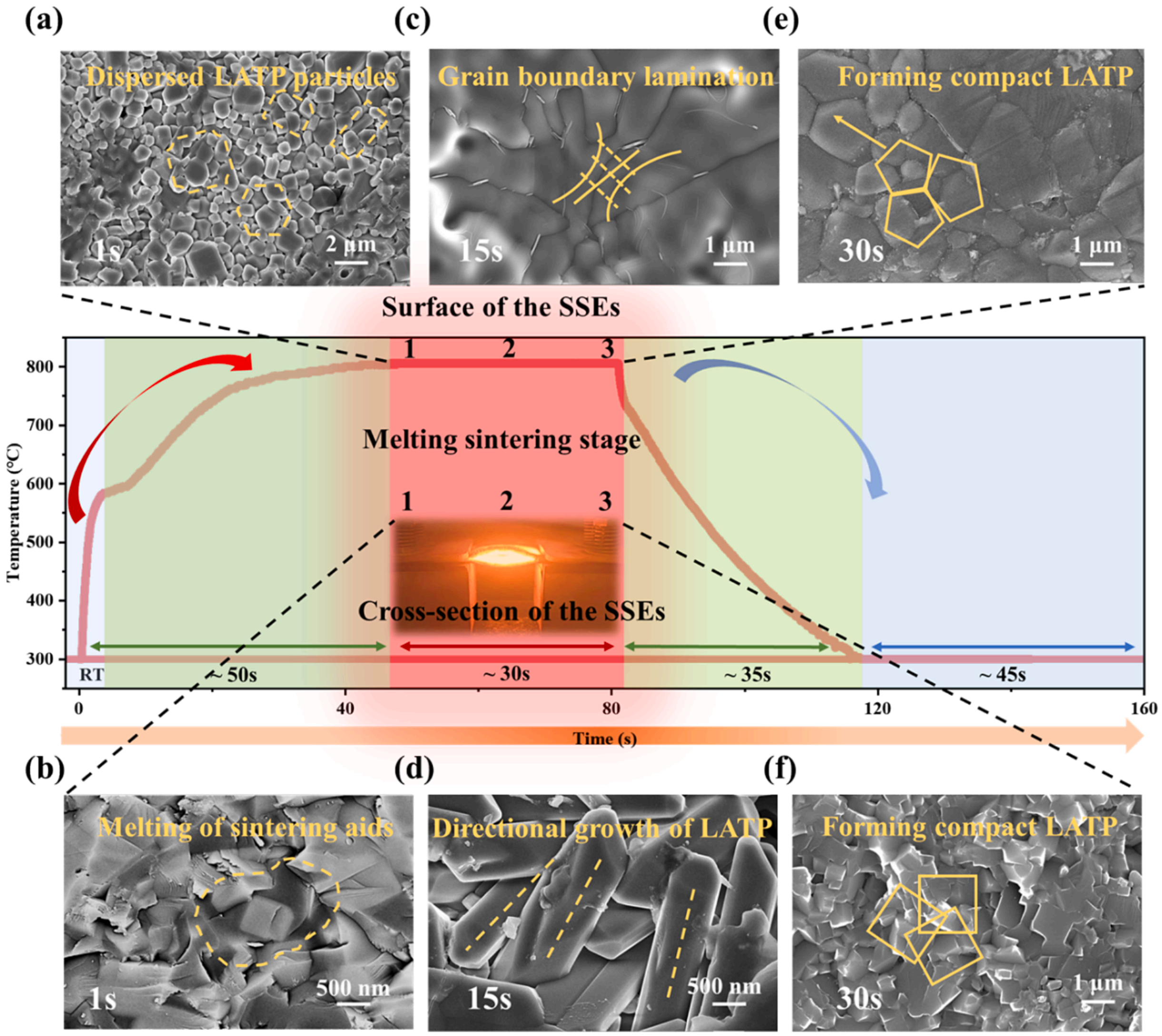

Fig. 3. Structural evolution of the LATP SSE during the Joule heating sintering process in NUHS. a-b) Surface and cross-sectional structures of the LATP SSE at 1 s into the melting sintering stage. c-d) Surface and cross-sectional structures of the LATP SSE at 15 s into the melting sintering stage. e-f) Surface and cross-sectional structures of the LATP SSE at 30 s into the melting sintering stage.

equivalent circuit in **Fig. S15**. The intercepts of the semicircle with the real axis at high and low frequencies corresponded to the bulk resistance (R_{bulk}) and total impedance (R_{tot}) of the SSEs. The R_{bulk} of LATP-NUHS was calculated as 280.6 ± 2.3 Ω, lower than that of LATP-CHST (363.5 ± 4.3 Ω) and LATP-CUHS (301.3 ± 10.6 Ω), indicating its lower bulk resistance resulting from the smaller microcrystal sizes. Although LATP-CUHS and LATP-NUHS exhibit similar R_{bulk} values, the introduction of sintering auxiliaries enhances the densification of LATP and fills the voids between ceramic particles. This results in a significantly lower R_{gb} for LATP-NUHS (392.7 ± 5.0 Ω) compared to LATP-CUHS (1715.6 ± 11.7 Ω). The detailed impedance and conductivity values of the LATP SSEs obtained from the impedance spectra were listed in Tables S1 and S2. LATP-NUHS achieved a total conductivity of 3.8×10^{-4} S cm^{-1}, which was also higher compared to LATP-CHST (2.1×10^{-4} S cm^{-1}) and LATP-CUHS (1.3×10^{-4} S cm^{-1}).

Besides, the Li^+ activation energy of LATP SSEs was quantitatively calculated using the Arrhenius equation. The Li^+ activation energy values for LATP-NUHS, LATP-CHST, and LATP-CUHS were 0.27 eV, 0.30 eV, and 0.37 eV, respectively (Fig. 5**b**). A lower activation energy corresponds to a lower energy barrier for lithium-ion transport. Further lithium-ion transference number (t_{Li^+}) tests revealed that LATP-NUHS exhibited the highest transference number (0.98) compared to LATP-CHST (0.96) and LATP-CUHS (0.91) (**Fig. S16**). A low t_{Li^+} can lead to rapid voltage decay during cycling due to concentration polarization. As a single-ion conductor, the t_{Li^+} of LATP should ideally approach 1. The reduced t_{Li^+} of LATP-CUHS may be attributed to the presence of a large number of electron-conductive defects, which contribute to the total charge transport [44]. In contrast, the introduction of ionic fillers effectively fills these electron-conductive defects with the single-ion conductor LiF, significantly suppressing electronic conduction in LATP-NUHS. The combination of lower lithium-ion energy barriers and fewer electron-conductive defects may explain the high lithium-ion conductivity of LATP-NUHS.

EIS tests on Li||LATP-NUHS||LFP batteries before and after TPW technique were further conducted (Fig. 5**c**), to evaluate the interface optimization strategy for integrated anode/SSE/cathode. The corresponding equivalent circuit models are shown in **Fig. S17**, where R_b represents the total resistance of LATP, interlayers, electrodes and battery packaging materials. R_{gb}, R_{int} and W_o correspond to the grain boundary resistance of LATP, the SSE/electrode interfacial resistance and Warburg impedance, respectively [45]. After thermal pulse welding, the interfacial resistance (R_{int}) of the Li||LATP-NUHS||LFP battery significantly decreased from 879.1 ± 4.3 Ω to 496.7 ± 3.7 Ω with the R_{gb} value remaining nearly constant. This result demonstrated that

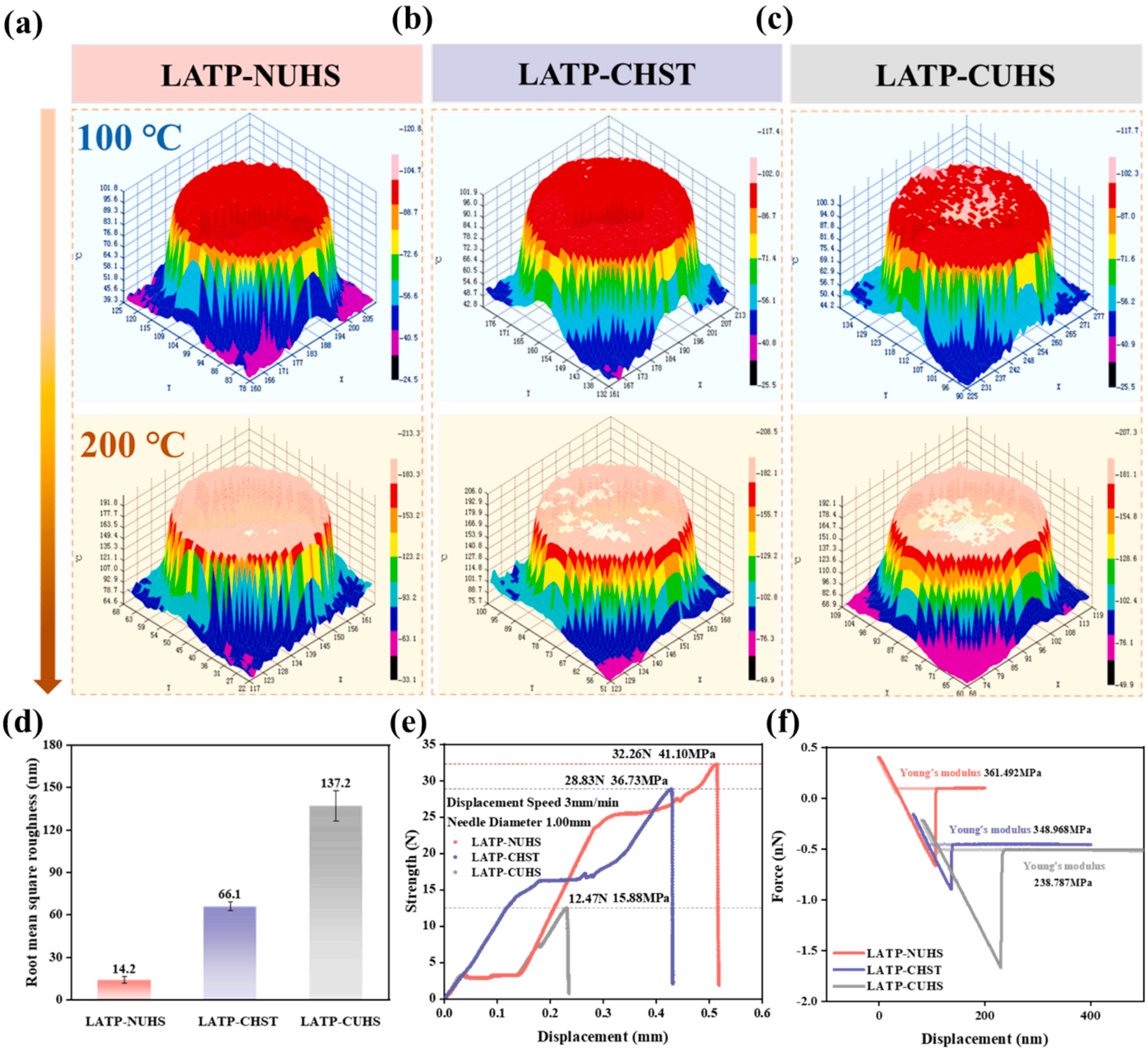

Fig. 4. Thermal, mechanical and surface roughness analysis of LATP SSEs. a-c) 3D infrared thermographic imaging under 100°C and 200°C for LATP-NUHS, LATP-CHST and LATP-CUHS. d) Root mean square roughness of LATP SSEs. Three times repeated experiments were carried out and the error bars were shown in Fig. 4d. e) Compressive stress–strain behavior of LATP SSEs. f) Young's modulus assessment via stress–strain curves of LATP SSEs.

thermal pulse welding could effectively improve the interface contact and reduce the interfacial resistance between the SSE and electrode, facilitating fast and stable interface ion transport.

To verify the improved interface contact for integrated anode/SSE/cathode after applying the TPW technique, the above Li||LATP-NUHS||LFP batteries were disassembled to observe LATP-NUHS/electrode interfaces. As shown in Fig. 5**d**, before applying the TPW technique, poor physical contact was observed at anode/LATP-NUHS interface, with a gap up to ~ 8 μm. After applying the TPW technique, the lithium foil was firmly bonded to the SSE surface with minimal overflow of molten lithium at the edges, which could effectively avoid potential short circuits. The interface contact between the composite cathode and the LATP-NUHS also plays an crucial role in interface ion transfer. As shown in Fig. 5**e**, the gaps at the cathode/LATP-NUHS interface were further reduced after treatment with the TPW technique. The active particles within the composite cathode were embedded more effectively into the micropores of LATP-NUHS, forming a continuous and dense network for ion and electron conduction.

Based on LATP-NUHS, LFP batteries fabricated by both the conventional physical stacking method (LATP-NUHS-CPS) and the TPW technique (LATP-NUHS-TPW) were subjected to 50 cycles at a high current density of 0.3 mA cm^{-2}. As shown in **Fig. S18,** the capacity of the Li||LATP-NUHS-CPS||LFP battery rapidly decayed below 50 mAh/g at 0.3 mA cm^{-2}. In contrast, the Li||LATP-NUHS-TPW||LFP battery maintained a capacity of over 100 mAh/g with a Coulombic efficiency exceeding 99 %. This result demonstrated that the tight SSE/electrode interface contact significantly enhances the rate capability of ASSLMBs. Following cycling, the LATP-NUHS-TPW SSEs were extracted, and their anode sides were examined. As illustrated in **Fig. S19**, the LATP-NUHS-CPS SSE underwent significant structural degradation after high-current cycling, whereas the LATP-NUHS-TPW maintained structural stability after 50 cycles, with only minimal secondary reaction products on the surface. Further analysis of the anode side of the LATP-NUHS-CPS SSE and LATP-NUHS-TPW SSE after 50 cycles was carried out by SEM (Fig. 5**f**), with energy-dispersive spectroscopy data presented in **Fig. S20**. Lithium deposition on the LATP-NUHS-TPW SSE was uniform with a smooth and well-defined solid electrolyte interphase (SEI) layer. However, the LATP-NUHS-CPS SSE displayed irregular lithium deposits and numerous micro-cracks during the lithium plating/stripping processes (Fig. 5**g**), compromising the structural integrity of SSE. These results demonstrate that the interface optimization strategy for integrated anode/SSE/cathode based on thermal pulse welding technology

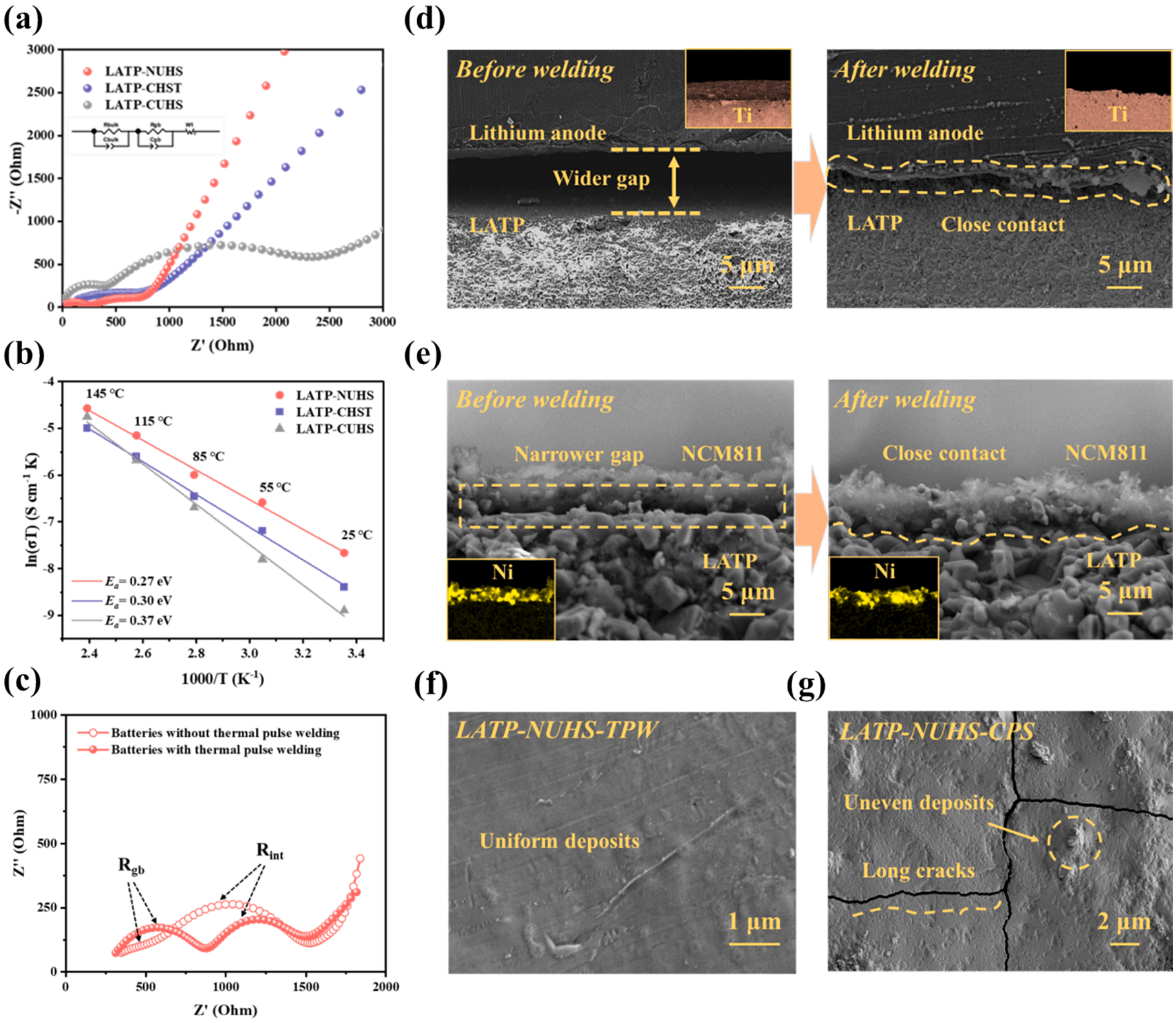

Fig. 5. Comparison of the ionic conductivity of various LATP SSEs and effects of the interface optimization strategy. a) EIS curves of various LATP SSEs in SP||LATP||SP batteries. Three times repeated experiments were carried out in Fig. 5a. b) Arrhenius plots and the activation energies (E_a) of LATP SSEs. c) EIS curves of the Li||LATP-NUHS||LFP batteries fabricated using CPS and TPW techniques. d) Anode/LATP-NUHS interface before and after applying TPW technique. e) Composite cathode/LATP-NUHS interface before and after applying the TPW technique. f-g) SEM images of the anode side of the LATP-NUHS-TPW and LATP-NUHS-CPS SSEs from Figure e after 50 cycles.

can significantly enhance the interface connection between SSE and electrode, further improving the uniformity of lithium deposition and strengthening the structural stability of ASSLMBs even under high-current cycling conditions.

Detailed electrochemical characterization and testing are presented in Fig. 6 to systematically verify the electrochemical performance of LATP-NUHS based on this integrated optimization strategy. The electrochemical windows of various LATP SSEs were measured via linear sweep voltammetry as shown in **Fig. S21**. Compared with LATP-CUHS exhibiting significant changes in response current between 3.59 V and 3.75 V, both LATP-CHST and LATP-NUHS exhibited a wide electrochemical window ranging from 2.5 to 6 V, ensuring their stable electrochemical behavior in high-voltage environments [46]. To evaluate the interfacial stability of lithium in prolonged contact with LATP and its ability to suppress lithium dendrites, we conducted repeated charge/discharge tests on Li||LATP||Li batteries at a current density of 0.1 mA cm^{-2} (Fig. 6**a**). Among the tested SSEs, LATP-NUHS exhibited the lowest overpotential of 58 mV after 250 h of cycling. In contrast, LATP-CUHS showed significant voltage polarization at 44 h, followed by an abrupt drop in overpotential at 47 h due to soft short-circuiting caused by continuous lithium dendrite penetration. When the current density was increased to 0.3 mA cm^{-2}, LATP-CHST demonstrated a rapid rise in internal resistance after multiple lithium dissolution-deposition cycles, resulting in short-circuit failure at 101 h (Fig. 6**b**). These results demonstrate the superior stability and dendrite suppression capability of LATP-NUHS for lithium anodes. Further cyclic voltammetry tests on Li||LATP||Cu batteries confirmed that lithium ions in LATP-NUHS could effectively deposit and strip on bare copper foil. Compared with LATP-CHST, LATP-NUHS showed higher response currents and a smaller redox potential gap (**Fig. S22**), indicating better reversibility and faster electrochemical reaction kinetics at the cathode side [47].

To assess the kinetic performance of LATP SSEs in LFP batteries, CV tests were performed on Li||LATP||LFP batteries at different scan rates. Figs. 6**c and S23** reveal distinct redox peaks for all three batteries, corresponding to lithium-ion intercalation and deintercalation in the LFP cathode. Among them, Li||LATP-NUHS-TPW||LFP exhibited the highest current response and less pronounced voltage polarization at higher scan rates, indicating superior reaction kinetics [48]. Fig. 6**d** showed a linear relationship between I_p and $\vartheta^{1/2}$ at scan rates ranging from 0.1 to 0.5 mV/s, consistent with the Randles-Sevcik equation, confirming that lithium-ion diffusion in the cathode is the rate-limiting step. As shown in **Table S3**, the $D_{\text{Li-reduction}}$ and $D_{\text{Li-oxidation}}$ values for Li||

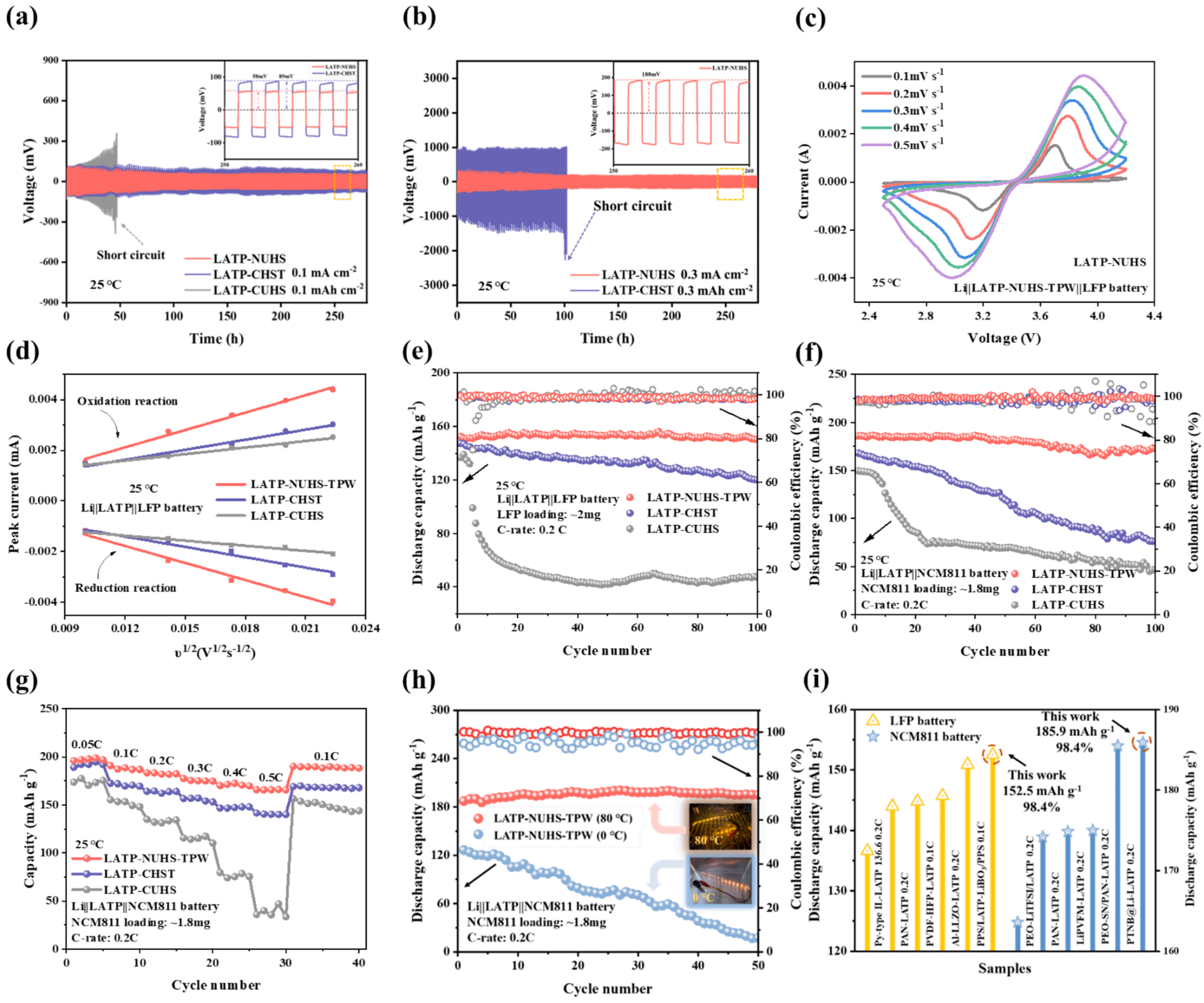

Fig. 6. Electrochemical characterization of various LATP SSEs. a) Constant current cycling performance of Li||LATP||Li batteries at 0.1 mA cm^{-2}. b) Constant current cycling performance of Li||LATP||Li batteries at 0.3 mA cm^{-2}. c) The CV curves of the Li||LATP-NUHS-TPW||LFP battery at different scan rates. d) $I_p - \vartheta^{1/2}$ relationship derived from the CV curves of Li||LATP||LFP batteries. e) Long-term cycling performance of Li||LATP||LFP at 0.2 C. f) Long-term cycling performance of Li||LATP||NCM811 at 0.2 C. g) Rate performance of Li||LATP||NCM811 from 0.05 C to 0.5 C. h) Long-term cycling performance of Li||LATP-NUS-TPW||NCM811 at 0 °C and 80 °C. i) Capacity comparison of ASSLMBs from recent literature with the ASSLMBs based on LATP-NUHS-TPW.

LATP-NUHS-TPW||LFP battery, derived from the $I_p - \vartheta^{1/2}$ relationship, are 1.7×10^{-10} cm^2/s and 1.8×10^{-10} cm^2/s, respectively, markedly surpassing the reported LFP batteries fabricated using the CPS method. This enhancement is likely due to the TPW technique, which densifies the cathode structure and improves ionic transfer at the interface, thereby accelerating the overall electrochemical reaction kinetics.

To systematically evaluate the impact of bulk and interface integration optimization on ASSLMBs, we conducted long-term cycling tests on Li||LATP||LiFePO$_4$ batteries with various LATP SSEs at 0.2C. LATP-NUHS-TPW exhibited the highest initial discharge capacity of 152.5 mAh/g with a prolonged charge–discharge plateau (**Fig. S24**). After 100 cycles, its polarization voltage could still remain stable ($\Delta E < 100$ mV) (**Fig. S25**). The capacity of LATP-NUHS-TPW (150.1 mAh/g) at 100 cycles was significantly higher than that of LATP-CHST (98.5 mAh/g) and LATP-CUHS (47.1 mAh/g), with a Coulombic efficiency of 98.5 % and a capacity retention rate of 98.4 % (Fig. 6**e**). In contrast, ASSLMBs with LATP-CUHS maintained only 34.4 % capacity retention after 100 cycles due to extensive grain boundaries and high interface ionic transfer impedance.

To evaluate the actual performance of various LATP SSEs under higher voltages (~4.2 V), we further assembled Li||LATP||NCM811 coin batteries for long-term cycling tests at 0.2C, and the results were displayed in Fig. 6**f** and **Fig. S26**. LATP-NUHS-TPW maintained the highest initial capacity of 185.9 mAh/g, with a capacity retention rate of 90.9 % after 100 cycles and a low polarization voltage during cycling (**Fig. S27**). At the 100th cycle, the specific capacity of LATP-NUHS-TPW remained at 168.1 mAh/g, significantly exceeding than that of LATP-CHST (76.7 mAh/g) and LATP-CUHS (46.3 mAh/g). Fig. 6**g** presents the rate performance and reversibility of various LATP SSEs, where LATP-NUHS-TPW possessed the highest specific capacity among these three LATP SSEs at charge–discharge rates ranging from 0.05C to 0.5 C. When the current density was reduced from 0.5 C to 0.1 C, the discharge specific capacity of LATP-CUHS could recover to 190.1 mAh/g again.

This integrated optimization strategy for bulk and interface also enabled ASSLMBs to operate across a wider temperature range. After being sealed in an oven (80 °C) or a refrigeration chamber (0 °C) for cycling, the optimized Li||LATP-NUHS-TPW||NCM811 batteries still successfully illuminated LED strips (Fig. 6**h**). In cyclic tests conducted in a temperature and humidity chamber, ASSLMBs demonstrated a Coulombic efficiency of over 90 % and stable cycling performance even at freezing temperatures. At an elevated temperature of 80°C, which is usually problematic for liquid batteries, the ASSLMBs achieved a specific capacity of 187.3 mAh/g and stable cycling (CE ~ 99 %) (Fig. 6**h**). These findings attested to the robust reliability of LATP-NUHS-TPW based batteries. In addition, compared with previously reported ASSLMBs based on LATP SSEs (Fig. 6**i, Table S4 and S5**), the ASSLMBs fabricated by this integrated optimization strategy better also exhibit better performance in both cycling capacity and stability, highlighting the practical potential of this integrated optimization strategy in future high-performance ASSLMBs.

4. Conclusion

In conclusion, an integrated optimization strategy was developed to address bulk-phase defects in LATP SSEs and interfacial contacts in ASSLMBs, leveraging the advanced Joule heating technique, thereby enabling a comprehensive improvement in the performance of ASSLMBs. In the optimization of bulk-phase defects in LATP SSEs, the addition of sintering auxiliaries (B_2O_3 and $LiBF_4$) enabled uniform ceramic particle arrangement during ultra-fast high-temperature sintering, yielding LATP SSEs with a crystallinity of 98.99 % and a defect rate as low as 0.01 %, along with excellent thermal stability and mechanical strength. In the optimization of interfacial contacts in ASSLMBs, high frequency thermal pulse welding technique via UHS ensured intimate anode/SSE/cathode contact (interfacial resistance reduced to $496.7 \pm 3.7\ \Omega$), enabling a unified ion-conducting network in ASSLMBs. As a result, both optimized LFP and NCM811 batteries through this integrated optimization strategy exhibited high initial capacities of 152.5 mAh/g (with a capacity retention rate of 98.4 % after 100 cycles at 0.2 C) and 185.9 mAh/g (with a capacity retention rate of 90.9 % after 100 cycles at 0.2 C), respectively, with a high application potential over a wide temperature range. This proposed novel integrated technique utilizing ultra-fast Joule heating sintering technique will provide a crucial technical reference for the efficient synthesis of advanced LATP SSEs and the broader application of Joule heating technology in the battery field.

Author contributions

S.S., J.W. and W.Y. conceived the concept and experiments. X.C., Z. G. and M.Z conducted the experiments. X.C., J.W. and C.L. carried out the electrochemical analysis. Z.G., J.Z. assisted in the fabrication and characterization of the samples. X.C. and M.Z. co-wrote the paper.

CRediT authorship contribution statement

Xiangming Cui: Writing – review & editing, Writing – original draft, Methodology, Investigation, Data curation, Conceptualization. **Xin Chen:** Writing – review & editing, Resources, Investigation. **Changzheng Lin:** Resources, Investigation. **Jingzhao Wang:** Resources, Investigation. **Zirui Guo:** Resources, Investigation. **Mi Zhou:** Resources, Investigation. **Zhouzhou Yao:** Resources, Investigation. **Jiaxin Zhang:** Resources, Investigation. **Shiyi Sun:** Writing – review & editing, Visualization, Resources, Investigation. **Jianan Wang:** Writing – review & editing, Visualization, Resources, Funding acquisition. **Wei Yan:** Resources, Investigation, Conceptualization.

Declaration of competing interest

The authors declare that they have no known competing financial interests or personal relationships that could have appeared to influence the work reported in this paper.

Acknowledgments

This work has been financially supported by the National Natural Science Foundation of China (52172097), New Energy Material Innovation Consortium Projects of Yunnan Province (202302AB080018), China Postdoctoral Science Foundation (2020M683467) The authors thank the Instrument Analysis Center at Xi'an Jiaotong University for their assistance with characterization analyses.

Appendix A. Supplementary data

Supplementary data to this article can be found online at https://doi.org/10.1016/j.jcis.2025.01.276.

Data availability

Data will be made available on request.

References

[1] N. Kittner, F. Lill, D.M. Kammen, Energy storage deployment and innovation for the clean energy transition, Nat. Energy 2 (2017).
[2] F. Degen, M. Winter, D. Bendig, J. Tuebke, Energy consumption of current and future production of lithium-ion and post lithium-ion battery cells, Nat. Energy 8 (2023) 1284–1295.
[3] H. Wang, D. Yu, C. Kuang, L. Cheng, W. Li, X. Feng, Z. Zhang, X. Zhang, Y. Zhang, Alkali Metal Anodes for Rechargeable Batteries, Chemistry 5 (2019) 313–338.
[4] Z.P. Shao, S.M. Haile, A high-performance cathode for the next generation of solid-oxide fuel cells, Nature 431 (2004) 170–173.
[5] C. Wang, K. Fu, S.P. Kammampata, D.W. McOwen, A.J. Samson, L. Zhang, G. T. Hitz, A.M. Nolan, E.D. Wachsman, Y. Mo, V. Thangadurai, L. Hu, Garnet-Type Solid-State Electrolytes: Materials, Interfaces, and Batteries, Chem. Rev. 120 (2020) 4257–4300.
[6] S. Ferrari, M. Falco, A.B. Munoz-Garcia, M. Bonomo, S. Brutti, M. Pavone, C. Gerbaldi, Solid-State Post Li Metal Ion Batteries: A Sustainable Forthcoming Reality? Adv. Energy Mater. 11 (2021).
[7] J. Janek, W.G. Zeier, Challenges in speeding up solid-state battery development, Nature, Energy 8 (2023) 230–240.
[8] L. Porz, T. Swamy, B.W. Sheldon, D. Rettenwander, T. Froemling, H.L. Thaman, S. Berendts, R. Uecker, W.C. Carter, Y.-M. Chiang, Mechanism of Lithium Metal Penetration through Inorganic Solid Electrolytes, Adv. Energy Mater. 7 (2017).
[9] D. Larcher, J.M. Tarascon, Towards greener and more sustainable batteries for electrical energy storage, Nat. Chem. 7 (2015) 19–29.
[10] H. Liu, X.-B. Cheng, J.-Q. Huang, H. Yuan, Y. Lu, C. Yan, G.-L. Zhu, R. Xu, C.-Z. Zhao, L.-P. Hou, C. He, S. Kaskel, Q. Zhang, Controlling Dendrite Growth in Solid-State Electrolytes, ACS Energy Lett. 5 (2020) 833–843.
[11] T. Sun, Q. Liang, S. Wang, J. Liao, Insight into Dendrites Issue in All Solid-State Batteries with Inorganic Electrolyte: Mechanism, Detection and Suppression Strategies, Small 20 (2024).
[12] M.J. Lee, J. Han, K. Lee, Y.J. Lee, B.G. Kim, K.-N. Jung, B.J. Kim, S.W. Lee, Elastomeric electrolytes for high-energy solid-state lithium batteries, Nature, 601 (2022) 217-+.
[13] C. Cao, Y. Li, Y. Feng, C. Peng, Z. Li, W. Feng, A solid-state single-ion polymer electrolyte with ultrahigh ionic conductivity for dendrite-free lithium metal batteries, Energy Storage Mater. 19 (2019) 401–407.
[14] L. Jia, J. Zhu, X. Zhang, B. Guo, Y. Du, X. Zhuang, Li-Solid Electrolyte Interfaces/Interphases in All-Solid-State Li Batteries, Electrochem. Energy Rev. 7 (2024).
[15] B. Wu, S. Wang, J. Lochala, D. Desrochers, B. Liu, W. Zhang, J. Yang, J. Xiao, The role of the solid electrolyte interphase layer in preventing Li dendrite growth in solid-state batteries, Energ. Environ. Sci. 11 (2018) 1803–1810.
[16] W. Xiao, J. Wang, L. Fan, J. Zhang, X. Li, Recent advances in $Li_{1+x}Al_xTi_{2-x}(PO_4)_3$ solid-state electrolyte for safe lithium batteries, Energy Storage Mater. 19 (2019) 379–400.
[17] P. Wu, W. Zhou, X. Su, J. Li, M. Su, X. Zhou, B.W.W. Sheldon, W. Lu, Recent Advances in Conduction Mechanisms, Synthesis Methods, and Improvement Strategies for $Li_{1+x}Al_xTi_{2-x}(PO_4)_3$ Solid Electrolyte for All-Solid-State Lithium Batteries, Adv. Energy Mater. 13 (2023).
[18] S. Chen, L. Nie, X. Hu, Y. Zhang, Y. Zhang, Y. Yu, W. Liu, Ultrafast Sintering for Ceramic-Based All-Solid-State Lithium-Metal Batteries, Adv. Mater. 34 (2022).
[19] J. Park, K.T. Bae, D. Kim, W. Jeong, J. Nam, M.J. Lee, D.O. Shin, Y.-G. Lee, H. Lee, K.T. Lee, Y.M. Lee, Unraveling the limitations of solid oxide electrolytes for all-solid-state electrodes through 3D digital twin structural analysis, Nano Energy 79 (2021).
[20] C. Wang, W. Ping, Q. Bai, H. Cui, R. Hensleigh, R. Wang, A.H. Brozena, Z. Xu, J. Dai, Y. Pei, C. Zheng, G. Pastel, J. Gao, X. Wang, H. Wang, J.-C. Zhao, B. Yang, X. Zheng, J. Luo, Y. Mo, B. Dunn, L. Hu, A general method to synthesize and sinter bulk ceramics in seconds, Science 368 (2020) 521.
[21] X. Zhao, W. Wu, Y. Bai, Y. Wu, J. Liu, P. Wang, H. Luo, K. Ren, Y. Song, H. Du, J. Deng, Microstructure evolution and densification behavior of ultrafast high-temperature sintered $Li_{6.5}La_3Zr_{1.5}Ta_{0.5}O_{12}$ ceramics, J. Power Sources 613 (2024).
[22] H. He, L. Wang, M. Al-Abbasi, C. Cao, H. Li, Z. Xu, S. Chen, W. Zhang, R. Li, Y. Lai, Y. Tang, M. Ge, Interface Engineering on Constructing Physical and Chemical Stable Solid-State Electrolyte Toward Practical Lithium Batteries, Energy Environ. Mater. 7 (2024).
[23] J. Sun, X. Yao, Y. Li, Q. Zhang, C. Hou, Q. Shi, H. Wang, Facilitating Interfacial Stability Via Bilayer Heterostructure Solid Electrolyte Toward High-energy, Safe and Adaptable Lithium Batteries, Adv. Energy Mater. 10 (2020).
[24] W. Zhou, S. Wang, Y. Li, S. Xin, A. Manthiram, J.B. Goodenough, Plating a Dendrite-Free Lithium Anode with a Polymer/Ceramic/Polymer Sandwich Electrolyte, J. Am. Chem. Soc. 138 (2016) 9385–9388.
[25] K. Shi, Z. Wan, L. Yang, Y. Zhang, Y. Huang, S. Su, H. Xia, K. Jiang, L. Shen, Y. Hu, S. Zhang, J. Yu, F. Ren, Y.-B. He, F. Kang, In Situ Construction of An Ultra-Stable

Conductive Composite Interface for High-Voltage All-Solid-State Lithium Metal Batteries, Angewandte Chemie-International Edition 59 (2020) 11784–11788.

[26] J. Jiang, Y. Ou, S. Lu, C. Shen, B. Li, X. Liu, Y. Jiang, B. Zhao, J. Zhang, In-situ construction of Li-Mg/LiF conductive layer to achieve an intimate lithium-garnet interface for all-solid-state Li metal battery, Energy Storage Mater. 50 (2022) 810–818.

[27] P. Bharathi, S.-F. Wang, Nanoscale Synthesis of $Li_{1.3}Al_{0.3}Ti_{1.7}(PO_4)_3$ Solid-State Lithium Ion Battery Electrolyte: A Structural and Ionic Conductivity Study, ACS Appl. Nano Mater. 7 (2024) 1615–1624.

[28] C. Luo, G. Zhao, M. Zhang, B. Wu, Q. Hua, Facile Route to Synthesize a Highly Sinterable $Li_{1.3}Al_{0.3}Ti_{1.7}(PO_4)_3$ Solid Electrolyte, ACS Appl. Mater. Interfaces 16 (2024) 3289–3301.

[29] D.-W. Lee, H.-S. Oh, R.-H. Lee, I.-H. Im, S.-H. Lee, Effect of Li_2O-B_2O_3-SiO_2 glass on Li plus diffusion and dendrite resistance of $Li_{6.1}Ga_{0.3}La_3Zr_2O_{12}$ solid-state electrolyte, Ceram. Int. 50 (2024) 2895–2900.

[30] X. Han, S. Wang, Y. Xu, G. Zhong, Y. Zhou, B. Liu, X. Jiang, X. Wang, Y. Li, Z. Zhang, S. Chen, C. Wang, Y. Yang, W. Zhang, J. Wang, J. Liu, J. Yang, All solid thick oxide cathodes based on low temperature sintering for high energy solid batteries, Energ. Environ. Sci. 14 (2021) 5044–5056.

[31] L. Dai, J. Wang, Z. Shi, L. Yu, J. Shi, Influence of $LiBF_4$ sintering aid on the microstructure and conductivity of LATP solid electrolyte, Ceram. Int. 47 (2021) 11662–11667.

[32] X. Yao, S. Chen, C. Wang, T. Chen, J. Li, S. Xue, Z. Deng, W. Zhao, B. Nan, Y. Zhao, K. Yang, Y. Song, F. Pan, L. Yang, X. Sun, Interface Welding via Thermal Pulse Sintering to Enable 4.6 V Solid-State Batteries, Adv. Energy Mater. 14 (2024).

[33] R. DeWees, H. Wang, Synthesis and Properties of NaSICON-type LATP and LAGP Solid Electrolytes, ChemSusChem 12 (2019) 3713–3725.

[34] S. Sun, J. Wang, S. Zong, Q. Ma, H. Li, X. Chen, X. Cui, K. Yang, Q. Cai, Y. Zhao, W. Yan, Integration Plasma Strategy Controlled Interfacial Chemistry Regulation Enabling Planar Lithium Growth in Solid-State Lithium Metal Batteries, Adv. Funct. Mater. 33 (2023).

[35] K. Waetzig, A. Rost, C. Heubner, M. Coeler, K. Nikolowski, M. Wolter, J. Schilm, Synthesis and sintering of $Li_{1.3}Al_{0.3}Ti_{1.7}(PO_4)_3$ (LATP) electrolyte for ceramics with improved Li^+ conductivity, J. Alloy. Compd. 818 (2020.).

[36] S. Sun, X. Cui, Q. Ma, J. Wang, M. Ma, X. Yao, Q. Cai, J. Li, X. Chen, Z. Wang, R. Zhuang, P. Mu, L. Zhu, J. Liu, W. Yan, Insight into the role of crystallinity in oxide electrolytes enabling high-performance all-solid-state lithium-sulfur batteries, J. Colloid Interface Sci. 650 (2023) 659–668.

[37] M. Hong, Q. Dong, H. Xie, X. Wang, A.H. Brozena, J. Gao, C. Wang, C. Chen, J. Rao, J. Luo, L. Hu, Tailoring grain growth and densification toward a high-performance solid-state electrolyte membrane, Mater. Today 42 (2021) 41–48.

[38] X. Gao, Y.-N. Zhou, D. Han, J. Zhou, D. Zhou, W. Tang, J.B. Goodenough, Thermodynamic Understanding of Li-Dendrite Formation, Joule 4 (2020) 1864–1879.

[39] Y. Zhu, X. He, Y. Mo, Origin of Outstanding Stability in the Lithium Solid Electrolyte Materials: Insights from Thermodynamic Analyses Based on First-Principles Calculations, ACS Appl. Mater. Interfaces 7 (2015) 23685–23693.

[40] D. Tewari, P.P. Mukherjee, Energetics Dictates Deposition at Metal/Solid Electrolyte Interfaces, J. Phys. Chem. C 125 (2021) 2221–2229.

[41] W. Ji, B. Luo, Q. Wang, G. Yu, Z. Liu, Z. Zhao, R. Zhao, S. Wang, X. Wang, B. Zhang, J. Zhang, F. Hou, J. Liang, Revealing the Influence of Surface Microstructure on Li Wettability and Interfacial Ionic Transportation for Garnet-Type Electrolytes, Adv. Energy Mater. 13 (2023).

[42] S.-G. Ling, J.-Y. Peng, Q. Yang, J.-L. Qiu, J.-Z. Lu, H. Li, Enhanced ionic conductivity in LAGP/LATP composite electrolyte, Chin. Phys. B 27 (2018).

[43] X. Lu, Y. Wu, D. Yang, R. Wang, Increased ionic conductivity of a NASICON lithium ion conductor under the influence of mesoporous materials, J. Alloy. Compd. 794 (2019) 585–593.

[44] H. Park, C. Bin Park, B.J. Sung, The effects of defects on the transport mechanisms of lithium ions in organic ionic plastic crystals, PCCP 25 (2023) 23058–23068.

[45] D. Ding, H. Tao, X. Fan, X. Yang, L.-Z. Fan, A Hybrid LiCl/Li_xSn Conductive Interlayer to Unlock the Potential of Solid-State Lithium Metal Batteries, Adv. Funct. Mater. 34 (2024).

[46] L. Luo, F. Zheng, H. Gao, C. Lan, Z. Sun, W. Huang, X. Han, Z. Zhang, P. Su, P. Wang, S. Guo, G. Lin, J. Xu, J. Wang, J. Li, C. Li, Q. Zhang, S. Wu, M.-S. Wang, S. Chen, Tuning the electron transport behavior at Li/LATP interface for enhanced cyclability of solid-state Li batteries, Nano Res. 16 (2023) 1634–1641.

[47] F. Han, Y. Zhu, X. He, Y. Mo, C. Wang, Electrochemical Stability of $Li_{10}GeP_2S_{12}$ and $Li_7La_3Zr_2O_{12}$ Solid Electrolytes, Adv. Energy Mater. 6 (2016).

[48] B.-N. Park, Unraveling Asymmetric Electrochemical Kinetics in Low-Mass-Loading $LiNi_{1/3}Mn_{1/3}Co_{1/3}O_2$ (NMC111) Li-Metal All-Solid-State Batteries, Materials 17 (2024).